nature geoscience

SUPPLEMENTARY INFORMATION

DOI: 10.1038/NGEO1826

A combination mode of the annual cycle and the El Niño/Southern Oscillation

Supplementary Information

Malte F. Stuecker[1,†],
Axel Timmermann[2],
Fei-Fei Jin[1,3,*],
Shayne McGregor[4,5]
& Hong-Li Ren[1,3]

1. Department of Meteorology, SOEST, University of Hawai'i at Manoa, Honolulu, HI, USA.
2. IPRC, SOEST, University of Hawai'i at Manoa, Honolulu, HI, USA.
3. Laboratory for Climate Studies, National Climate Center, China Meteorological Administration, Beijing, China.
4. CCRC, University of New South Wales, Sydney, NSW, Australia.
5. ARC Centre of Excellence for Climate System Science, University of New South Wales, Sydney, Australia.

[*]jff@hawaii.edu

[†]stuecker@soest.hawaii.edu

Full Methods

Empirical Orthogonal Functions Empirical Orthogonal Functions (EOFs) represent the dominant patterns (in terms of variance) of spatio-temporal variability of a dataset. An EOF analysis[S1] is performed on the monthly ERA-40[S2] 10 m wind anomalies for the period 1958-2001 and the spatial domain from 10°S-10°N and 100°E-60°W. The regressed zonal and meridional wind anomalies are plotted on a larger domain (30°S-30°N) for better visualization of the large-scale patterns (Fig. 1a-d). For the model ensemble experiments (see paragraph "Atmospheric General Circulation Model Experiments"), we perform an EOF analysis on the individual ensemble members and average their respective Principal Components (PCs). The normalised averaged PCs are regressed onto the ensemble mean 10 m wind anomaly fields to obtain their corresponding EOF pattern. Furthermore, we perform the same EOF analysis on the 10 m wind anomalies from the 500 year pre-industrial control run from the GFDL CM2.1 climate model[S3,S4]. The EOF pattern and composite PC time evolution (Supplementary Figs. 6,8) are very similar to the observations (Fig. 1a-d, Supplementary Fig. 3).

Spectral Analysis For the Blackman-Tukey (BT) spectral method[S5] we use a Bartlett window size of 11 years (Fig. 2, Supplementary Figs. 2b, 5, 9a-b). The equivalent degrees of freedom for the BT method can be estimated as $\nu = 2(n/m - 1/3)$, where n denotes the time series length and m the window length[S5]. For the Multi-Taper method (MTM) spectral method[S6,S7] we use 3 (Supplementary Figs. 1,2c) or 5 tapers (Supplementary Fig. 9c-d).

Assuming that the basic redness of the SST boundary conditions[S8] also reddens the atmospheric wind response, we test the BT and MTM PC2 wind spectra against the null hypothesis of an autoregressive model of order one (AR(1)) and calculate the respective 95% confidence intervals (99% for Supplementary Fig. 9c-d) assuming a χ^2 distribution.

To enhance the signal-to-noise ratio of the PC2 time series, we perform a Singular-Spectrum Analysis (SSA)[S6] on the observed wind PC2 (PC2 OBS). We then use the first 20 components to reconstruct the time series (PC2 REC), which acts essentially as a low-pass filter. The spectra exhibit clear $1 - f_{\mathrm{E}}$ difference tone peaks (Supplementary Fig. 2).

The mean squared coherence between the PC2s (Supplementary Fig. 10) is calculated using the Welch spectral method[S9] and a window size of 11 years (Supplementary Fig. 10a-c) or 33 years (Supplementary Fig. 10d). The 95% confidence intervals are calculated using bootstrapping (n=1000). We find significant spectral coherence at the combination tone frequency bands when comparing the PC2s (Supplementary Fig. 10).

To test the robustness of our results, an alternative null hypothesis is used. We identify the non-combination tone features by subtracting $\mathrm{PC2_{SIMPLE}}$ (the lowest order theoretical approximation to the combination mode) from PC2 $\mathrm{EXP_A}$ and calculate the corresponding spectrum (Supplementary Fig. 11). This spectrum is basically white with a small red component. We determine the estimated atmospheric white noise level and use it as a null hypothesis against which we test the PC2 $\mathrm{EXP_A}$ combination tone peaks. We find that the PC2 $\mathrm{EXP_A}$ combination tone peaks are well above the atmospheric noise level

(Supplementary Fig. 11). Hence, we are able to reject both the red noise (Fig. 2b) and white noise (Supplementary Fig. 11) null hypotheses.

Atmospheric General Circulation Model Experiments To test the combination mode hypothesis we conduct a sensitivity experiment EXP_A with the Atmospheric General Circulation Model (AGCM) AM2.1[S10]. The model, used here in a horizontal resolution of 2° latitude and 2.5° longitude, simulates atmospheric dynamics and thermodynamics realistically when forced with observed SST[S10]. The main objective of the experiment is to quantify the effect of ENSO-related SST anomalies in combination with the SST climatology on the atmospheric circulation. The ENSO single spatial forcing pattern for AM2.1 is derived by regressing the normalised ERA-40[S2] 10 m wind anomaly PC1 on the monthly SST anomalies (1958-2001) obtained from the Hadley centre sea ice and Sea Surface Temperature (HadISST1) data set[S11]. The resulting SST pattern is then multiplied by the normalised ERA-40 wind PC1 to obtain the full spatio-temporal evolution of the temperature field linearly related to the interannual ENSO mode. These SST anomalies are then added on the observed climatological mean annual cycle of SST taken from the Reynolds Optimum Interpolation (OI) SST dataset[S12]. To enhance the signal-to-noise-ratio of our analysis, a 10 member ensemble (identical forcing but perturbed atmospheric initial conditions) of AM2.1 hindcast experiments is conducted using the described SST boundary conditions from 1958 to 2001. As we are only interested in the interaction of interannual SST anomaly variations with the annual cycle, all other atmospheric parameters are kept at constant 1982 values (e.g. greenhouse gas concentrations and aerosols). Both EOF1 and EOF2 pattern (Fig. 1a-d) and the corresponding PC time evolution (Fig. 1e-f) are captured well by the model simulation compared to observations. The main EOF2 pattern difference between the model experiment and observations is that the simulated Philippine anticyclone is slightly shifted westward and features a reduced amplitude.

Furthermore, we conduct an additional single member sensitivity experiment over the same period with the same ENSO SST anomaly forcing described above but without a seasonal cycle (PERP). The climatological SSTs and radiative forcing are both kept constant at perpetual autumn equinox conditions, however the ENSO SST anomalies are varying in time exactly as in the sensitivity experiments above. PC2 shows no characteristic phase shift during boreal winter (Supplementary Fig. 3) and no correlation with the observed PC2 (r=0.05), thus demonstrating that the mean annual cycle of SST is a key element for the atmospheric combination mode response. As expected, the corresponding EOF2 does not exhibit the zonal wind anomalies characteristic of the southward wind shift (Supplementary Fig. 4), although it captures parts of the Philippine anticyclone structure (The anticyclone however is confined to the far western Pacific and the zonal wind pattern is quasi-symmetric throughout most of the domain).

To further verify the combination mode hypothesis we conduct another experiment (EXP_B) using ENSO-related SST anomalies and the seasonal cycle from the GFDL CM2.1 500 year pre-industrial control run[S3,S4], which simulates ENSO dynamics reasonably well[S4]. We calculate the CM2.1 single spatial SST anomaly pattern by regressing the normalised

CM2.1 10m monthly wind anomaly PC1 on the monthly CM2.1 SST anomalies. To obtain the temporal evolution of the forcing we multiply the pattern with the CM2.1 wind PC1. These anomalies are then added to the CM2.1 SST annual cycle. All other atmospheric parameters are again kept constant (same as in experiment $\mathrm{EXP_A}$). The AM2.1 AGCM is then integrated for 150 years and an EOF analysis is performed on the AGCM 10 m wind anomalies. The simulated EOF1 and EOF2 pattern (Supplementary Fig. 6), corresponding PC time evolution (Supplementary Figs. 7,8) and spectra (Supplementary Figs. 9,10) show very good agreement with the first 150 years of the coupled CM2.1 run.

These experiments will enable us to further elucidate the importance of different annual cycle/ENSO interaction mechanisms[9−22,S13−S25].

El Niño Composites of the Principal Components To highlight the contribution of PC2 to the El Niño phase transition, we generate a composite of the PCs for the three strongest wind PC2 anomaly events (1982/83, 1991/92, 1997/98) with respect to the annual cycle evolution (Supplementary Fig. 3). The rapid phase switch of the simulated wind PC2 at the end of the calendar year is captured well in the composite El Niño among all ensemble members and their average as well as by $\mathrm{PC2_{SIMPLE}}$. It is accompanied by a southward shift of the westerly wind anomalies, which is known to terminate El Niño event and leads to the development of the Philippine anticyclone (Fig. 1b,d). The simulated PC2 and $\mathrm{PC2_{SIMPLE}}$ show a faster recovery to negative values compared to the observed PC2. This is explained by the dominance of the slower $1 - f_{\mathrm{E}}$ combination tone peak in observations compared to the dominant faster $1 + f_{\mathrm{E}}$ peak in the simulation (Fig. 2). Furthermore, we generate another composite of the PCs for the 18 strongest El Niño events with respect to the annual cycle evolution for both the CM2.1 run and $\mathrm{EXP_B}$ (Supplementary Fig. 8).

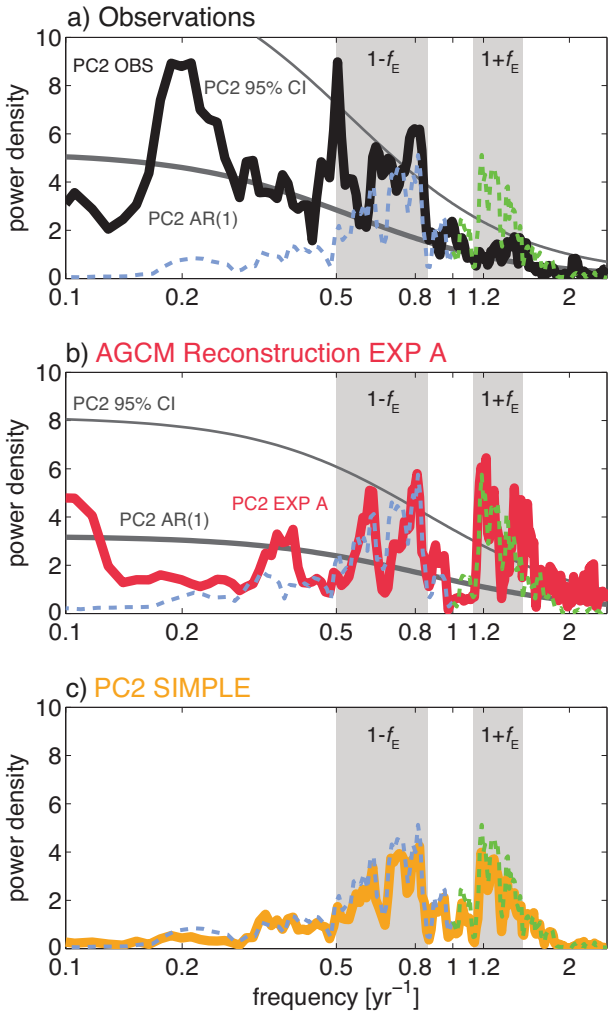

Supplementary Figure 1: Power spectra for PC2 using the Multi-Taper method (MTM). Frequency is abbreviated by f. To illustrate the PC2 combination tone frequencies, PC1 was shifted to $1 - f$ (dashed blue) and $1 + f$ (dashed green) and scaled by a factor 1/3. Grey boxes indicate the near-annual combination tone frequency bands $1 - f_{\mathrm{E}}$ and $1 + f_{\mathrm{E}}$. The AR(1) null hypothesis for the PC2s in (a)-(b) is displayed by a thick grey line and the 95% confidence interval (CI) indicated by a thin grey line. **(a)** Observed PC2 and frequency-shifted PC1s. **(b)** Averaged experiment $\mathrm{EXP_A}$ PC2 and frequency-shifted PC1s. **(c)** $\mathrm{PC2_{SIMPLE}}$ and frequency-shifted PC1s.

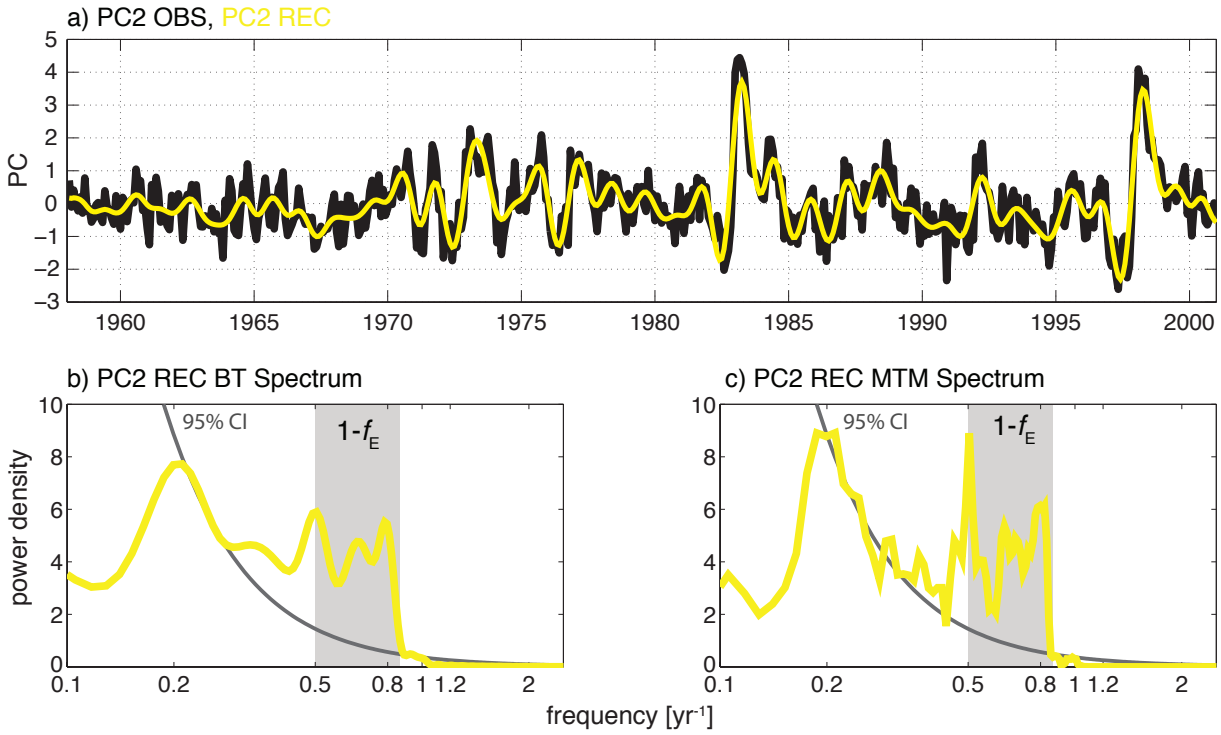

Supplementary Figure 2: **(a)** Normalised observed PC2 (PC2 OBS; black) and SSA-reconstructed observed PC2 (PC2 REC; yellow). **(b)** Power spectrum for PC2 REC using the Blackman-Tukey (BT) method. **(c)** Power spectrum for PC2 REC using the Multi-Taper method (MTM). The grey box indicates the near-annual combination tone frequency band $1 - f_{\mathrm{E}}$. The 95% confidence intervals (CI) for both spectra are indicated by thin grey lines.

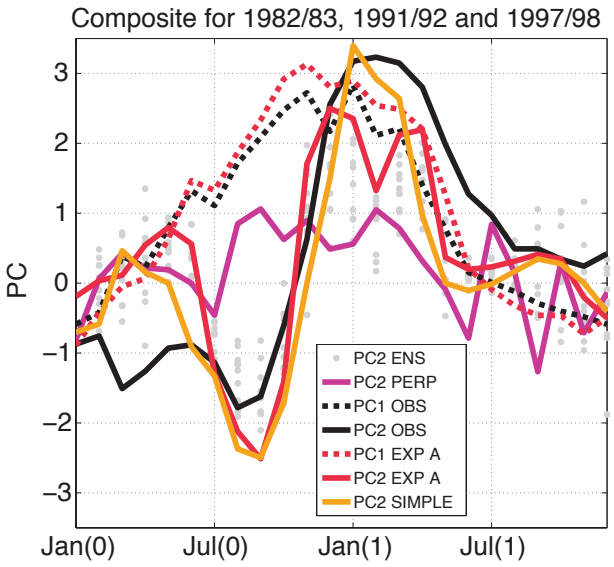

Supplementary Figure 3: Normalised PC1 (dashed) and PC2 (solid) composites of the strongest wind PC2 anomaly events (1982/83, 1991/92 and 1997/98) for both the observed 10 m wind anomalies (black) and the AGCM average of all ensemble member PCs (red). Further, the PC2 composite of the perpetual autumn equinox experiment (solid magenta), the individual ensemble member $\mathrm{EXP_A}$ PC2 composites (grey dots) and the $\mathrm{PC2_{SIMPLE}}$ time series (solid orange) are shown. Note that the amplitude of the normalised PC2 averaged over the ensemble members (solid red) has an increased amplitude compared to the normalised individual member PC2s (grey dots) during the El Niño composite due to the reduced noise in the average for the neutral and negative ENSO phase. In the composite year 0 denotes the developing phase and year 1 the decaying phase.

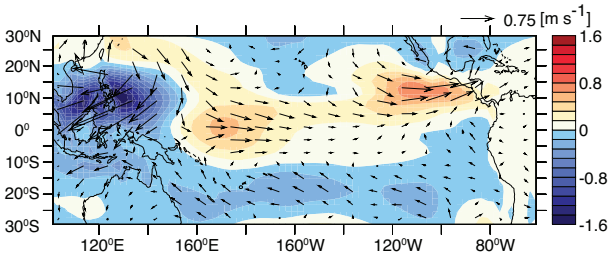

Supplementary Figure 4: EOF2 pattern of the 10 m wind anomalies from the perpetual autumn equinox experiment (12% explained variance). The unit for the zonal wind speed (shading) and 10 m wind vectors is [m s^{-1}].

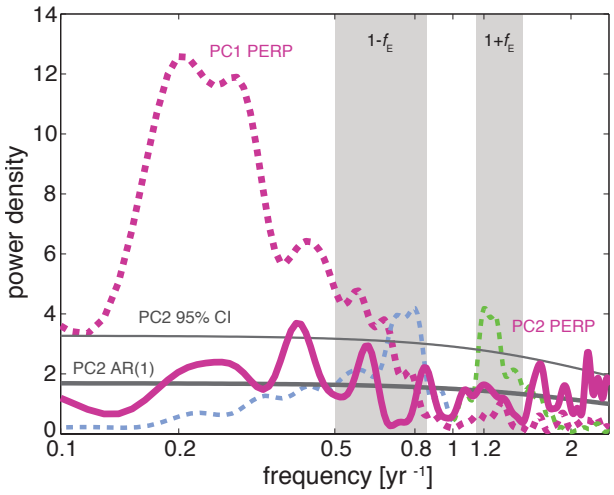

Supplementary Figure 5: Power spectrum for the perpetual autumn equinox experiment PC1 (dashed magenta) and PC2 (solid magenta) using the Blackman-Tukey (BT) method. Frequency is abbreviated by f. To illustrate the hypothetical location of the PC2 combination tone frequencies, PC1 was shifted to $1 - f$ (dashed blue) and $1 + f$ (dashed green) and scaled by a factor 1/3. The grey boxes indicate the near-annual combination tone frequency bands $1 - f_{\mathrm{E}}$ and $1 + f_{\mathrm{E}}$. The AR(1) null hypothesis for PC2 is displayed by a thick grey line and the 95% confidence interval (CI) indicated by a thin grey line.

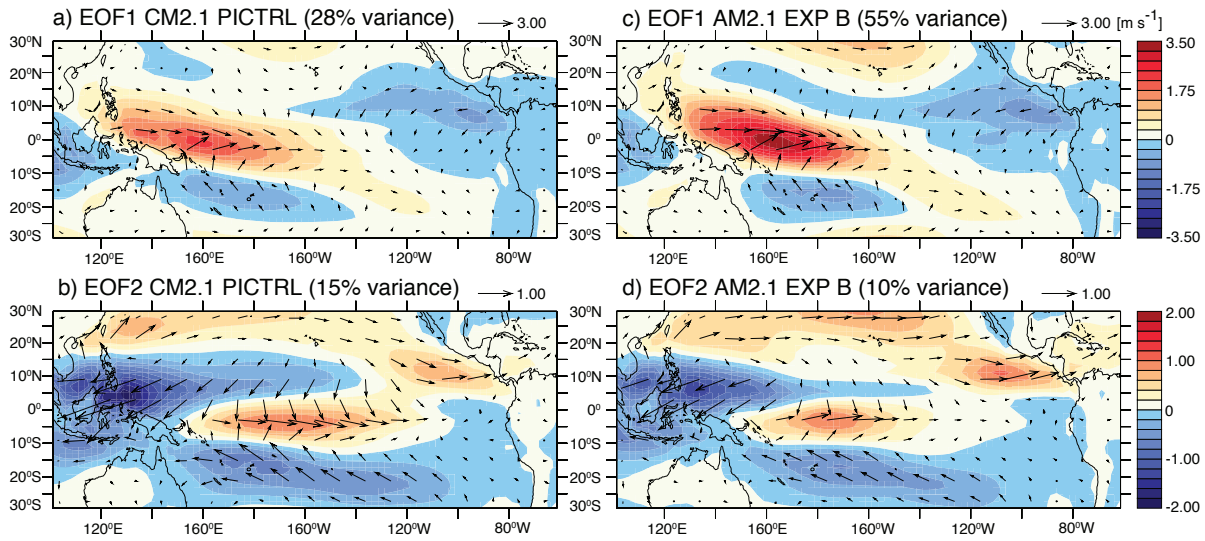

Supplementary Figure 6: **(a)-(d)** Dominant pattern of wind variability (zonal wind as shading) in the tropical Pacific obtained by an EOF decomposition of 10 m wind anomalies for the GFDL CM2.1 500 year pre-industrial control run and a 150 year forced AM2.1 AGCM experiment (EXP_B).

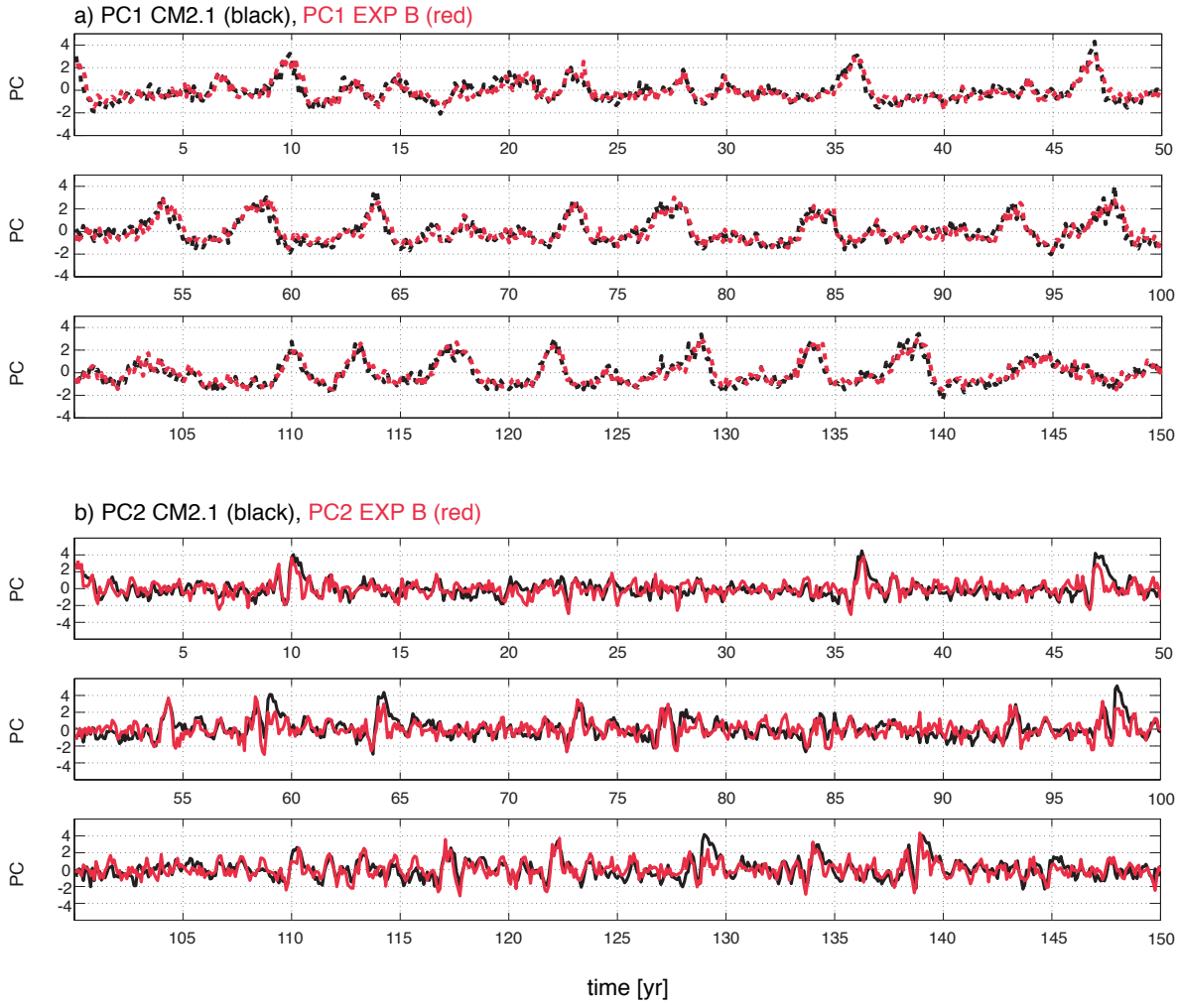

Supplementary Figure 7: **(a)** Normalised PC1 time series for CM2.1 (black; only first 150 years displayed) and the AGCM experiment (red; EXP_B). **(b)** Normalised PC2 time series for CM2.1 (black; only first 150 years displayed) and the AGCM experiment (red; EXP_B).

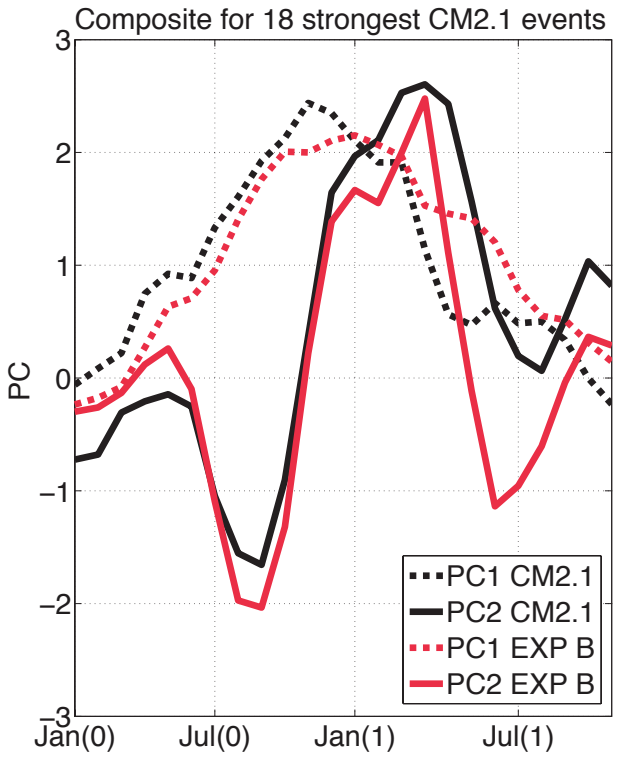

Supplementary Figure 8: Normalised PC1 (dashed) and PC2 (solid) composites of the 18 strongest El Niño events in the first 150 years of both the CM2.1 pre-industrial control (black) and the 150 year AM2.1 experiment (red) using the ENSO-related CM2.1 SST anomalies forcing (EXP_B). Year 0 denotes the developing phase and year 1 the decaying phase.

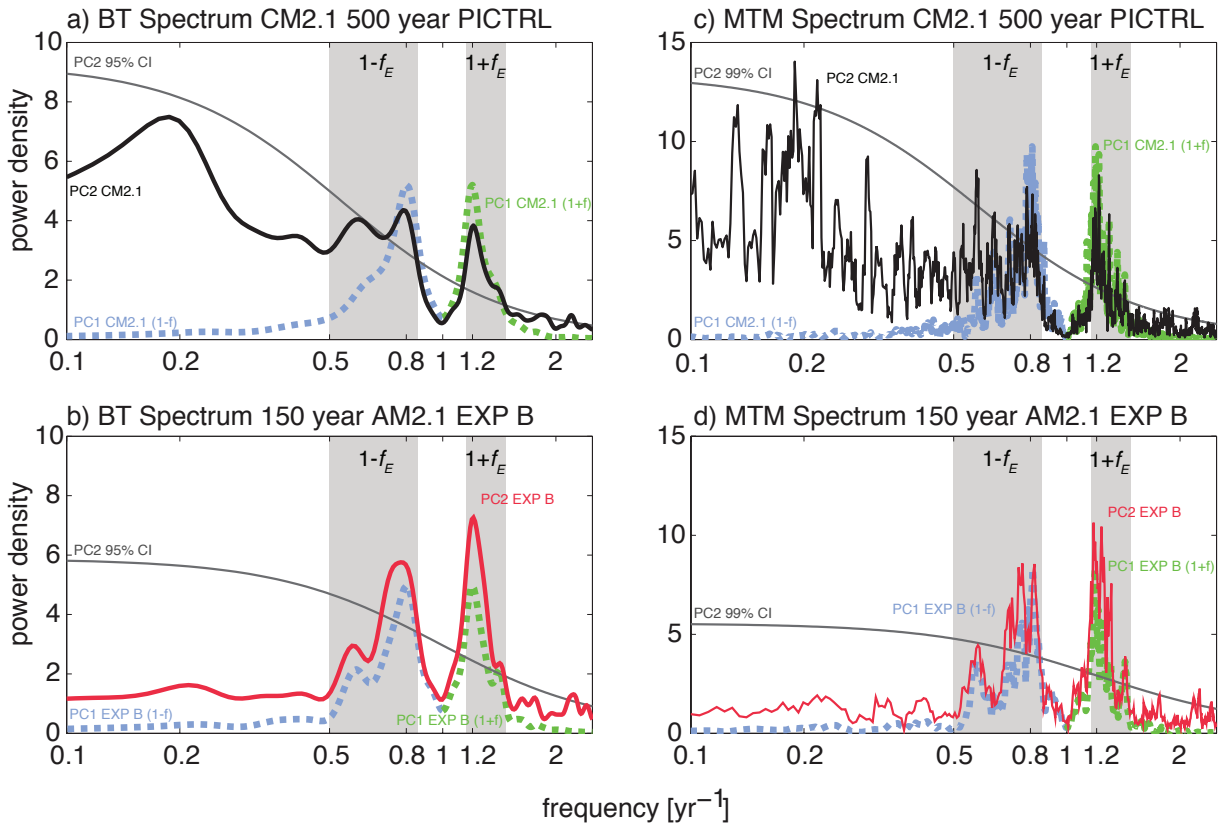

Supplementary Figure 9: Power spectra for the simulated 10m wind anomalies PCs using the Blackman-Tukey (BT) method **(a-b)** and the Multi-Taper method (MTM) **(c-d)**. Frequency is abbreviated by f. To illustrate the PC2 combination tone frequencies, PC1 was shifted to $1 - f$ (light blue dashed lines) and $1 + f$ (light green dashed lines) and their amplitudes scaled by a factor 1/4. Grey boxes indicate the near-annual combination tone frequency bands $1 - f_{\mathrm{E}}$ and $1 + f_{\mathrm{E}}$. The 95% confidence interval (CI) for the BT spectra and the 99% CI for the MTM spectra are indicated by thin grey lines. **(a)** BT spectrum for the 500 year CM2.1 pre-industrial control PC2 (solid black). **(b)** BT spectrum for the 150 year AM2.1 AGCM experiment ($\mathrm{EXP_B}$) PC2 (solid red). **(c)** MTM spectrum for the 500 year CM2.1 pre-industrial control PC2 (solid black). **(d)** MTM spectrum for the 150 year AM2.1 AGCM experiment ($\mathrm{EXP_B}$) PC2 (solid red).

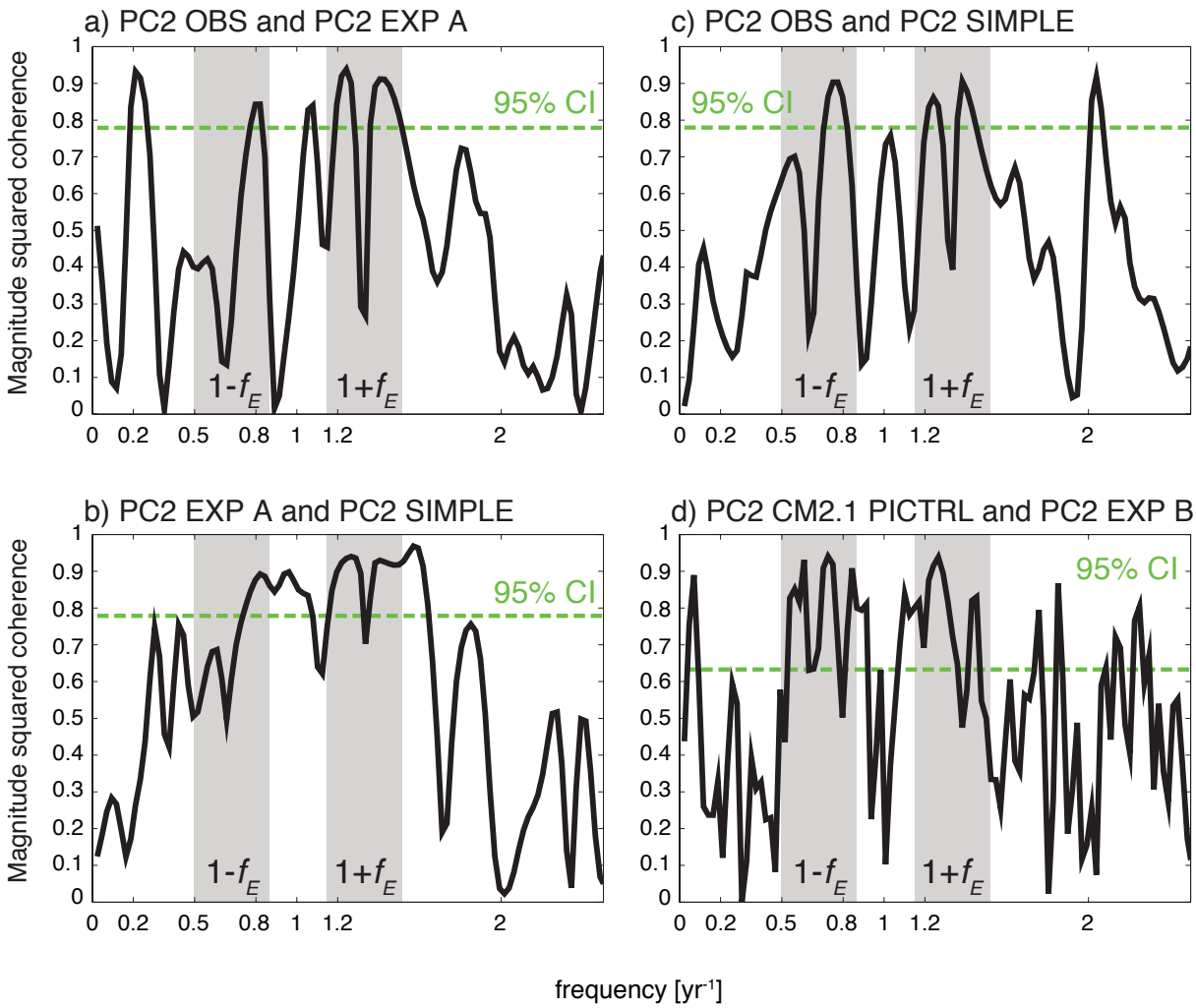

Supplementary Figure 10: Mean squared coherence for the 10m wind anomalies PC2s using the Welch spectral method. The respective 95% confidence intervals were estimated using bootstrapping. **(a)** Coherence between observed PC2 and the ensemble mean experiment (EXP_A) PC2. **(b)** Coherence between the ensemble mean experiment (EXP_A) PC2 and $PC2_{SIMPLE}$. **(c)**. Coherence between observed PC2 and $PC2_{SIMPLE}$. **(d)** Coherence between the first 150 years of the CM2.1 pre-industrial control PC2 and the 150 year AGCM experiment using the ENSO-related CM2.1 SST anomalies forcing (EXP_B).

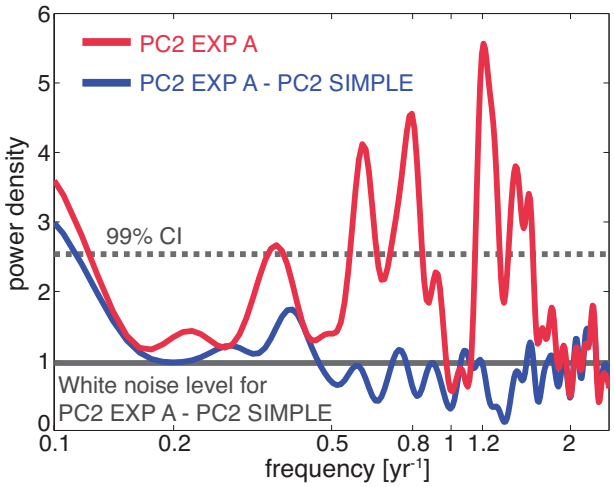

Supplementary Figure 11: Blackman-Tukey spectrum for PC2 $\mathrm{EXP_A}$ (red line) and PC2 $\mathrm{EXP_A} - \mathrm{PC2_{SIMPLE}}$ (blue line) with the atmospheric white noise level corresponding to the latter (solid grey line) and the associated 99% confidence interval (dashed grey line).

Supplementary References

S1. Lorenz, E. N. *Empirical Orthogonal Functions and Statistical Weather Prediction* (MIT, 1956)

S2. Uppala, S. M. et al. The ERA-40 re-analysis. *Q. J. R. Meteorol. Soc.* **131**, 2961-3012 (2005). Doi:10.1256/qj.04.176

S3. Delworth, T. L. et al. GFDL's CM2 global coupled climate models - Part 1: Formulation and simulation characteristics. *J. Climate* **19**, 643-674 (2006)

S4. Wittenberg, A. et al. GFDL's CM2 global coupled climate models - Part 3: Tropical Pacific climate and ENSO. *J. Climate* **19**, 698-722 (2006)

S5. Blackman, R. B. & Tukey, J. W. *The Measurement of Power Spectra* (Dover Publications, 1958)

S6. Ghil, M. et al. Advanced spectral methods for climatic time series. *Rev. Geophys.* **40**, 3.1-3.41 (2002)

S7. Thomson, D. J. Spectrum estimation and harmonic analysis. *Proceedings of the IEEE* **70**, 1055-1096 (1982)

S8. Hasselmann, K. Stochastic climate models Part I. Theory. *Tellus* **28**, 473-485 (1976)

S9. Welch, P. D. The Use of Fast Fourier Transform for the Estimation of Power Spectra: A Method Based on Time Averaging Over Short, Modified Periodograms. *IEEE Trans. Audio Electroacoust.* **AU-15**, 70-73 (1967)

S10. The GFDL Global Atmospheric Model Development Team. The New GFDL Global Atmosphere and Land Model AM2-LM2: Evaluation with Prescribed SST Simulations. *J. Climate* **17**, 4641-4673 (2004). Doi:10.1175/JCLI3223.1

S11. Rayner, N. A. et al. Global analyses of sea surface temperature, sea ice, and night marine air temperature since the late nineteenth century. *J. Geophys. Res.* **108** (2003). Doi:10.1029/2002JD002670

S12. Reynolds, R. W. & Smith, T. M. Improved global sea surface temperature analyses using optimum interpolation. *J. Climate* **7**, 929-948 (1994)

S13. Wang, X. L. The Coupling of the Annual Cycle and ENSO Over the Tropical Pacific. *J. Atmos. Sci.* **51**, 1115-1136 (1994)

S14. Tziperman, E. et al. Irregularity and Locking to the Seasonal Cycle in an ENSO Prediction Model as Explained by the Quasi-Periodicity Route to Chaos. *J. Atmos. Sci.* **52**, 293-306 (1995)

S15. Tziperman, E. et al. Mechanisms of Seasonal - ENSO interaction. *J. Atmos. Sci.* **54**, 61-71 (1997)

S16. Tziperman, E. et al. Locking of El Niño's Peak Time to the End of the Calendar Year in the Delayed Oscillator Picture of ENSO. *J. Climate* **11**, 2191-2199 (1998)

S17. Neelin, J. D. et al. Variations in ENSO Phase Locking. *J. Climate* **13**, 2570-2590 (2000)

S18. Galanti E. & Tziperman, E. ENSO's Phase Locking to the Seasonal Cycle in the Fast-SST, Fast-Wave, and Mixed-Mode Regimes. *J. Atmos. Sci.* **57**, 2936-2950 (2000)

S19. Galanti E. et al. The Equatorial Thermocline Outcropping - A Seasonal Control on the Tropical Pacific Ocean - Atmosphere Instability Strength. *J. Climate* **15**, 2721-2739 (2002)

S20. An, S.-I. & Wang, B. Mechanisms of Locking of the El Niño and La Niña Mature Phases to Boreal Winter. *J. Climate* **14**, 2164-2176 (2001)

S21. Yan, B. L. & Wu, R. G. Relative roles of different components of the basic state in the phase locking of El Nino mature phases. *J. Climate* **20**, 4267-4277 (2007)

S22. Lengaigne, M. and Vecchi, G. A. Contrasting the termination of moderate and extreme El Niño events in Coupled General Circulation Models. *Clim. Dyn.* (2009) Doi:10.1007/s00382-009-0562-3

S23. Xiao, H. & Mechoso, C. R. Seasonal Cycle-El Niño Relationship: Validation of Hypotheses. *J. Atmos. Sci.* **66**, 1633-1653 (2009)

S24. Stein, K. et al. Seasonal Synchronization of ENSO Events in a Linear Stochastic Model. *J. Climate* **23**, 5629-5643 (2010). Doi:10.1175/2010JCLI3292.1

S25. Ham, Y.-G. et al. What controls phase-locking of ENSO to boreal winter in coupled GCMs? *Clim. Dyn.* (2012). Doi:10.1007/s00382-012-1420-2